CHAPTER 6

$Fe_{(100-x)}Ni_{(x)}$ NANOCRYSTALLINE ALLOY POWDER SYNTHESIS BY AUTO-COMBUSTION ROUTE FOLLOWED BY HYDROGEN REDUCTION

The development of nanocrystalline alloy powder synthesis is a useful technique to achieve better properties than conventionally available alloy powders. These properties may include better mechanical, thermal, electrical and electrochemical properties. In the present chapter, the focus is on the synthesis of nanocrystalline $Fe_{(100-x)}Ni_{(x)}$ alloy powders. In the previous chapters 4 and 5, commercially available Fe and Ni powders have been used for synthesizing Fe-Ni alloys and composites. In the present chapter, the sol-gel auto-combustion route followed by hydrogen reduction is used for synthesizing Fe-Ni alloy powder. Although this is a quick synthesis route for the synthesis of nano powders of alloy, yet it has not been used extensively for the synthesis of Fe-Ni nanoparticles.

The present chapter describes the synthesis of Fe-Ni alloy powder and its characterization. The detailed synthesis process is already described in chapter 3 (Section 3.2.1). The oxide powder is obtained by auto-combustion which was then ground and reduced at 700°C/1h in a hydrogen atmosphere. Three different compositions with nomenclature A-($Fe_{90}Ni_{10}$), A-($Fe_{70}Ni_{30}$) and A-($Fe_{50}Ni_{50}$) are synthesized using the above route.The powder characterization methods such as XRD, SEM, TEM, and MPMS have been used for confirming the formation of nanocrystalline alloy powder.

6.1 X-ray Diffraction (XRD)

Auto-combustion synthesis route is an exothermic reaction between an oxidizer and a reducer. In the present work, citric acid is acting as a fuel as well as a complexing agent for the cations present in nitrates solution. Oxygen in nitrates acts as an oxidizer. Fig. 6.1 displays the XRD patterns of the oxide precursor powders after auto-combustion for x= 10, 30 and 50 mole% compositions. The powders are crystalline in nature. It is observed that the formed powders are comprised of $NiFe_2O_4$ (JCPDS 10-0325), NiO (JCPDS 44-1159) and α-Fe_2O_3(JCPDS 33-0664). With increasing nickel nitrate content, XRD peaks of $NiFe_2O_4$ become sharper. A few peaks of Ni (JCPDS 04-0850) are also observed. This may be due to the reduction of NiO to Ni as a result of citric acid's carbonization in the presence of air atmosphere.

For the reduction process, all the three prepared compositions were kept in a quartz tube furnace and reduced in hydrogen atmosphere at 700°C for 1h. The oxide powders formed after auto-combustion were converted into alloy powder after reduction.

Fig. 6.2 shows the phase analysis of (a) A-($Fe_{90}Ni_{10}$), (b) A-($Fe_{70}Ni_{30}$) and (c) A-($Fe_{50}Ni_{50}$) alloy powders after the reduction of oxide powders.The analysis is done using Rietveld refinement. Rietveld refinement of all the compositions is done using Fm-3m and Im-3m space groups. FULLPROF software [128] is used for the structural refinement. Structural parameters resulting from Rietveld refinement are listed in Table 6.1. γ phase is matched with JCPDS 47-1405, and α is matched with JCPDS 37-0474. The crystallite size of the alloy powders calculated using Scherrer formula which is found in nano range for all the three compositions (Table 6.1).

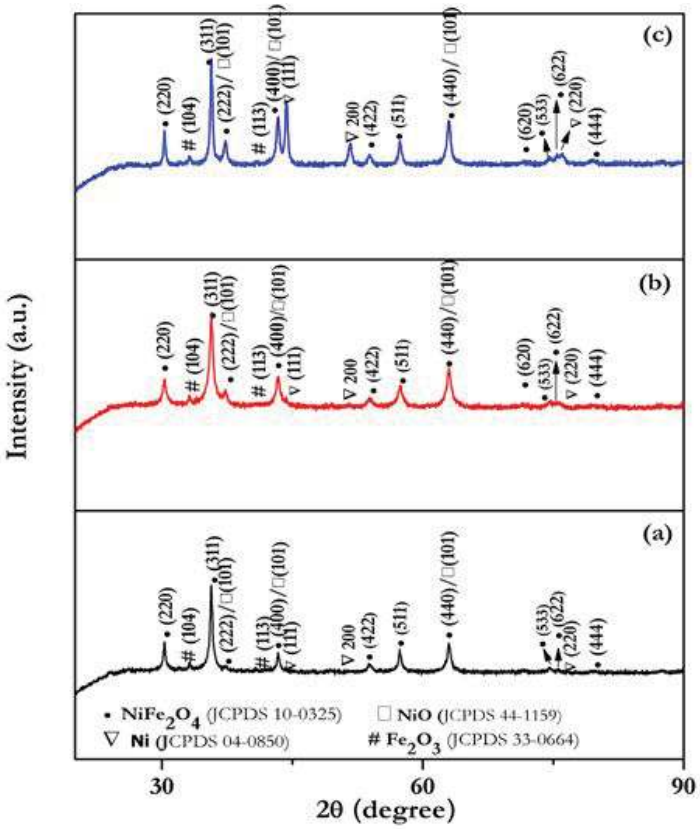

FIGURE 6.1: X-ray diffraction patterns of oxide powders after auto-combustion for the compositions with (a) x= 10 mole%, (b) x=30 mole% and (c) x=50 mole%.

Fig. 6.3 shows the Fe-Ni phase diagram reported by Swartzendruber [109]. According to this phase diagram, α- phase dominates below 10 wt.% Ni while heating up to $\sim$900°C and cooling. A small region of γ also exists in this composition and temperature range. Above 10 wt.% Ni, γ phase starts forming at relatively lower temperature. At around 30 wt.% Ni, complete γ phase forms above 500°C which changes to (α+γ) phase during cooling. Complete γ phase forms in 50 wt.% Ni composition. Therefore reduction of formed oxide powders at 700°C resulted in the formation of γ and α-(Fe,Ni) alloys. This is in good agreement with the reported Fe-Ni phase diagram.

In the present work, it is evident from XRD analysis that BCC α-(Fe,Ni) is formed

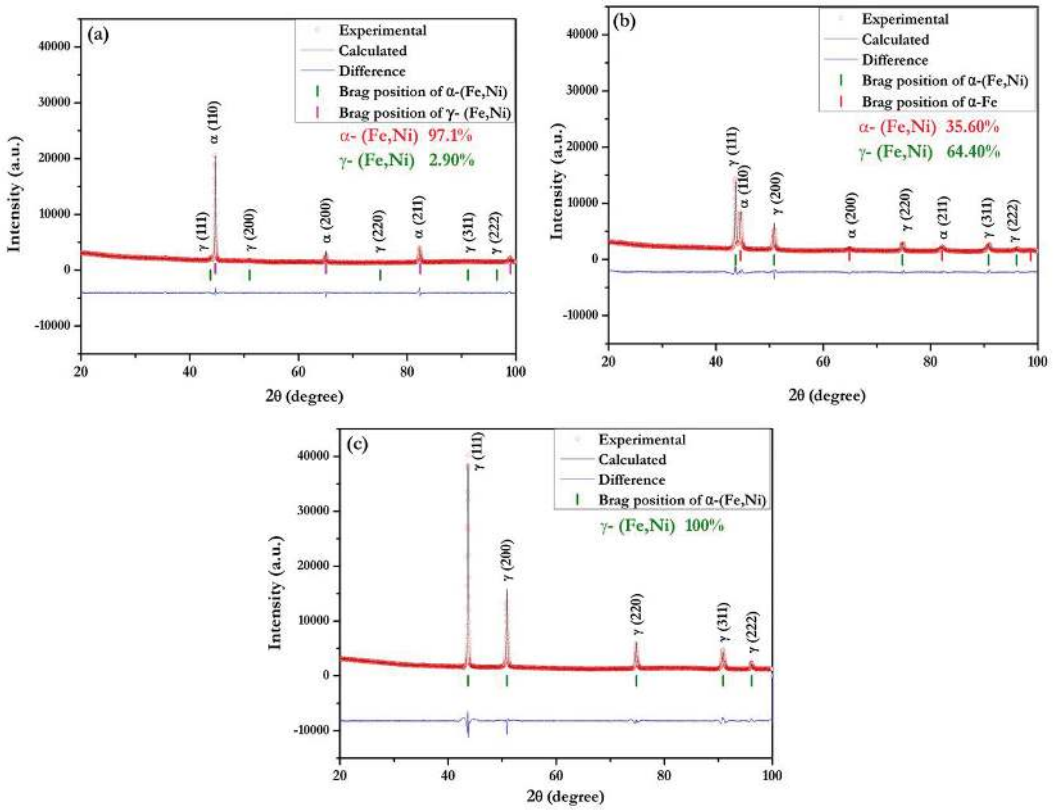

FIGURE 6.2: Rietveld refinement of (a) A-($Fe_{90}Ni_{10}$), (b) A-($Fe_{70}Ni_{30}$) and (c) A-($Fe_{50}Ni_{50}$).

in A-($Fe_{90}Ni_{10}$) alloy powder as a major phase whereas the small peak of FCC γ-(Fe,Ni) is also identified. Quantitative amount of γ and α-(Fe,Ni) phases determined from the Rietveld analysis is listed in Table. 6.1. In this method, least square refinements are done for obtaining the best fit. This is based on the experimental and refined structural models. From Fig. 6.2 (a-c), it is evident that experimentally observed pattern (black line) fits very well with the crystallographic patterns (red dots) with negligible fitting residue (R-Ro). Peaks of γ-(Fe,Ni) phase become prominent with increasing Ni content. Formation of more γ phase in A-($Fe_{70}Ni_{30}$) powder is indicated by the increased relative intensity of its stronger XRD peaks. Therefore, significant peaks of both α and γ phases are present in

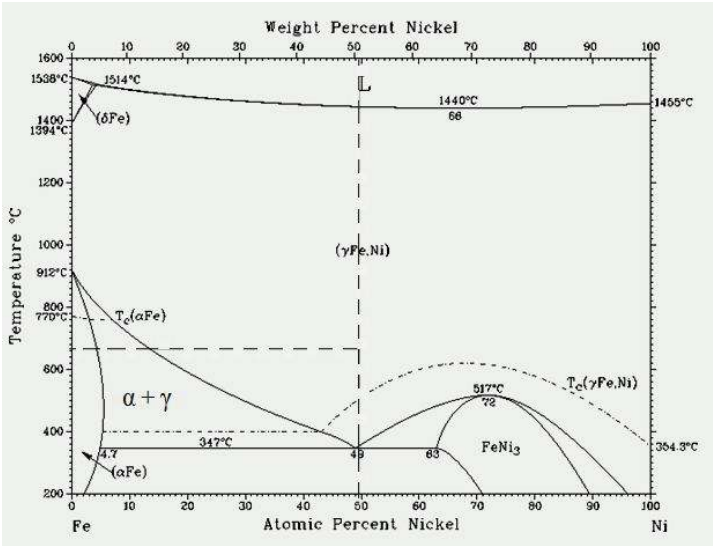

FIGURE 6.3: Fe-Ni phase diagram [109].

TABLE 6.1: Refined structural parameters for all the compositions.

S. No	Composition	Crystallite size (nm)	Bragg-R factor	R_f-factor	Rexp	χ^2	Lattice parameter ($\mathring{A}$)	
							$\alpha-$ (Fe,Ni)	$\gamma-$ (Fe,Ni)
1	$Fe_{90}Ni_{10}$	36.0	2.53	3.40	2.37	2.07	2.8686	3.5825
2	$Fe_{70}Ni_{30}$	34.2	2.78	3.58	2.28	2.46	2.8675	3.5841
3	$Fe_{50}Ni_{50}$	34.0	3.95	6.55	2.33	7.92	-	3.5860

A-($Fe_{70}Ni_{30}$) powder. Complete γ phase formation is achieved in A-($Fe_{50}Ni_{50}$) powder for which no peak of α- phase is present in its XRD pattern.

6.2 Scanning Electron Micrographs (SEM)

SEM micrographs of combusted powder with x=(a)10, (b)30 and (c)50 mole% is shown in Figs. 6.4. Citric acid as a fuel reduces the reaction time due to very high temperature attained during combustion. This also disperses the powder obtained by the auto-combustion reaction. Tiny pores are also observed in the microstructures which are generated due to the escape of gases during ignition (reaction of citric acid and nitrates for oxide formation). This makes the powder loosely bound and puffy in nature.

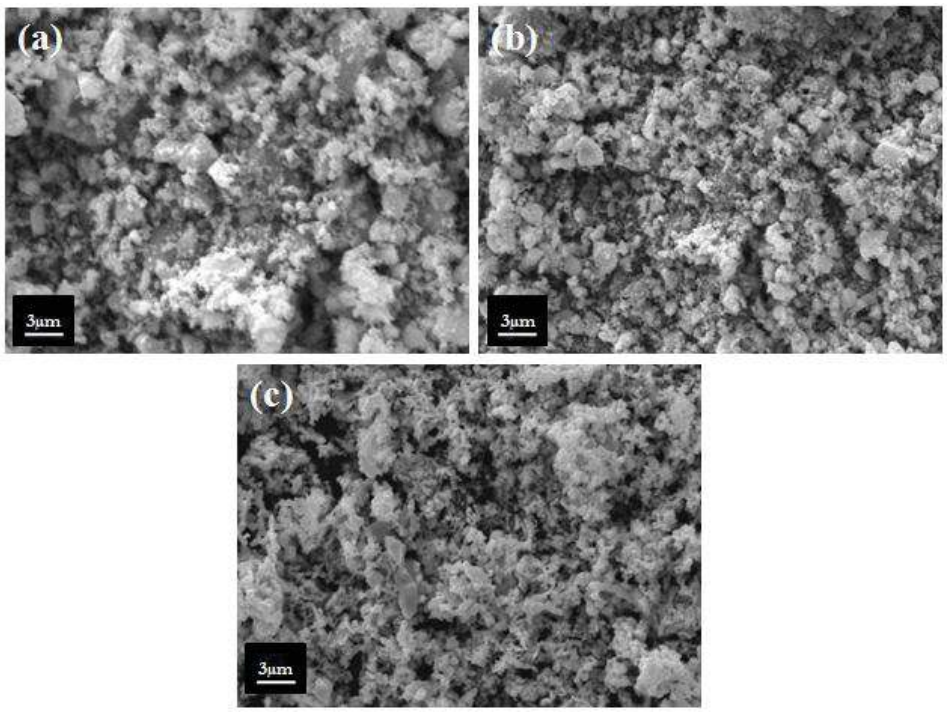

FIGURE 6.4: Scanning electron micrographs of oxide powders after auto-combustion for the compositions with (a) x= 10 mole%, (b) x=30 mole% and (c) x=50 mole%.

Figs. 6.5 (a-c) show the SEM microstructures of obtained powders after reduction. It is observed that the spherical and smooth particle surfaces along with small pores are present in powders after reduction. Formation of a network structure between spherical

particles is observed as a result of agglomeration in powders. From the elemental analysis, complete γ-(Fe,Ni) phase formation is observed in A-($Fe_{50}Ni_{50}$) composition. There is no evidence for the presence of oxygen in any alloy powder from EDX analysis. It is concluded that the crystallites of nanocrystalline powder join to make a continuous structure which would help in increasing the final density.

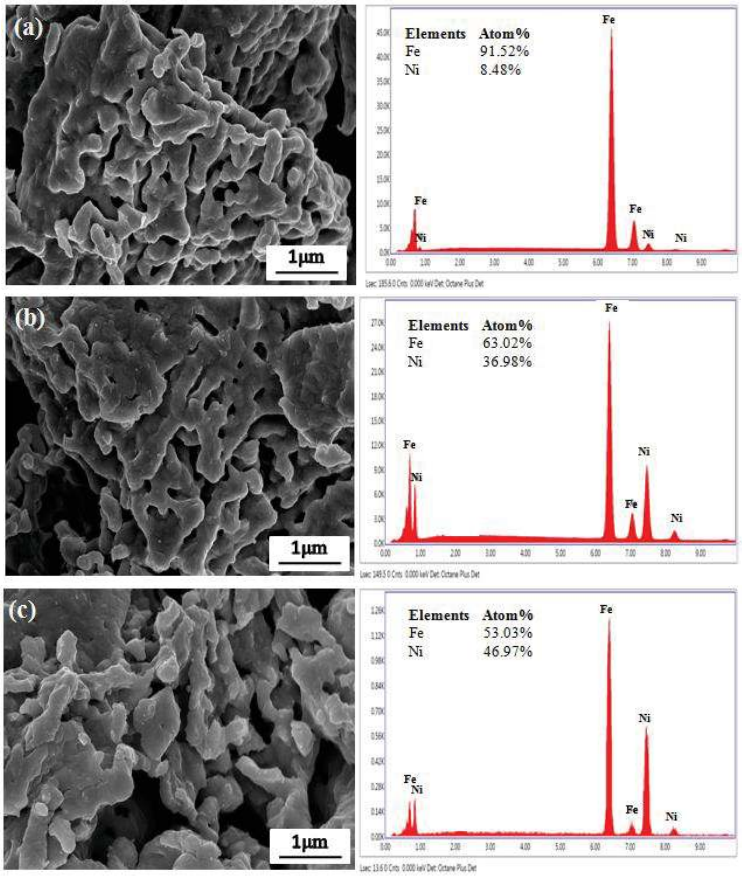

FIGURE 6.5: Scanning electron micrographs of (a) A-($Fe_{90}Ni_{10}$), (b) A-($Fe_{70}Ni_{30}$) and (c) A-($Fe_{50}Ni_{50}$) powders.

6.3 Transmission Electron Micrographs (TEM)

Figs. 6.6 (a-c) show the TEM images of A-($Fe_{90}Ni_{10}$), A-($Fe_{70}Ni_{30}$) and A-($Fe_{50}Ni_{50}$) powders, respectively and Fig. 6.6 (d) shows the SAED (selected area electron diffraction) pattern of A-($Fe_{50}Ni_{50}$) reduced powder. The Microscope FEI TECNAI G^2 was used for micrographs and selected area diffraction (SAED) pattern. It is already discussed

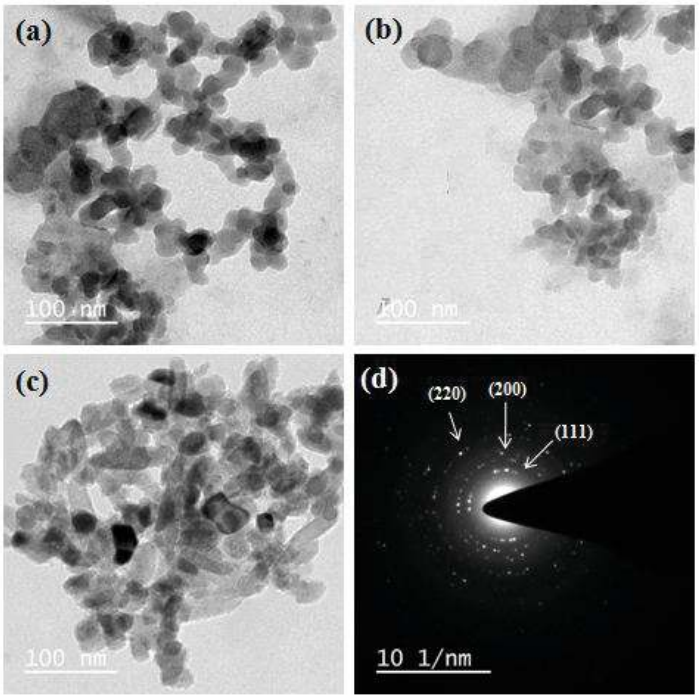

FIGURE 6.6: Transmission electron micrographs of (a) A-($Fe_{90}Ni_{10}$), (b) A-($Fe_{70}Ni_{30}$) and (c) A-($Fe_{50}Ni_{50}$) powders.

from SEM analysis that the nanosize powders formed a continuous network during powder reduction. Using TEM analysis, the formation of the nanoparticles network with clear boundaries is confirmed in A-($Fe_{90}Ni_{10}$) powder. A change in morphology with varying Ni content is observed. The agglomeration in the nanoparticles network started in composition A-($Fe_{70}Ni_{30}$) and complete agglomeration of nanoparticle network is observed in

A-($Fe_{50}Ni_{50}$) reduced powder. The nanocrystalline powders of all the three compositions are found to have particles less than 50 nm. The analysis of SAED pattern confirms the presence of nanocrystalline γ-(Fe,Ni) phase in A-($Fe_{50}Ni_{50}$) alloy powder. This is also confirmed by the XRD results [Fig. 6.2 c].

6.4 Magnetic Measurements

Table. 6.2 lists the coercivity and saturation magnetization values for obtained Fe-Ni alloy powders. Fig. 6.7 shows the magnetization curves of nanocrystalline $Fe_{(100-x)}Ni_{(x)}$ alloy powders. Magnetic measurements were made using an MPMS 3, EM-QM vibrating sample magnetometer at room temperature. It is reported by Buschow et al. [129] that the random fluctuation of magneto-crystalline anisotropy in amorphous and nanocrystalline materials occur on a smaller scale than the domain wall width. This leads to disappearing of magnetic anisotropy and excellent soft magnetic behavior. From the random anisotropic model [130], the coercivity of nanocrystalline soft magnetic materials varies as 1/D for grain size smaller than magnetic exchange length $L_{exch} \sim$ 40-50 nm where D is the crystallite size. In the present work, the average crystallite size of all the synthesized Fe-Ni alloy powders is in a range 34 to 36 nm, and hence all three curves exhibit soft ferromagnetic behavior with small hysteresis loops at room temperature. The magnetization curves [Fig. 6.7] in response to the external applied magnetic field (15 kOe) give Ms and Hc for all synthesized alloy powders. With increasing Ni content from 10 to 50%, Ms decreases from 181.4 to 108.6 emu/g and Hc increases from 4.90 to 28.5 Oe. The variation in Ms and Hc can also be explained by their dependence on the powder morphology

[Fig. 6.6] and its correlation with peak intensity ratio of (111) and (110) [Fig. 6.2]. It is expected that the particles were oriented in (110) direction at lower Ni content. Increasing Ni content resulted in a decrease in (110) peak intensity and agglomeration of network structure with increased particles alignment in (111) direction.

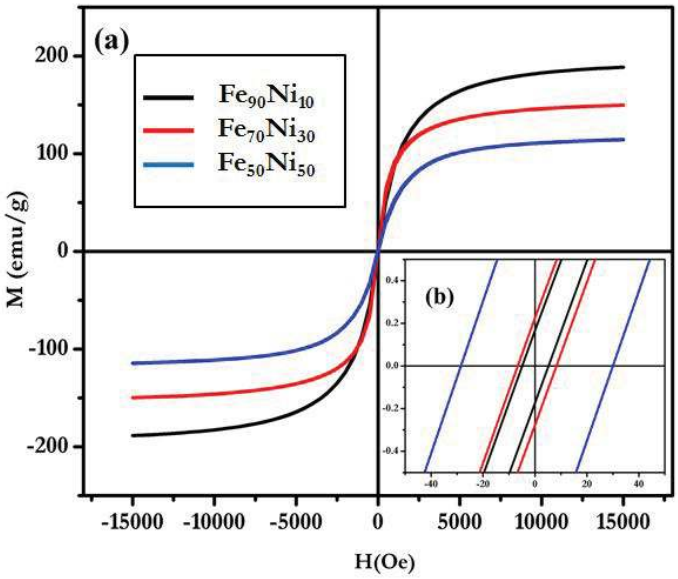

FIGURE 6.7: Magnetic hysteresis loops of (a) A-($Fe_{90}Ni_{10}$), (b) A-($Fe_{70}Ni_{30}$) and (c) A-($Fe_{50}Ni_{50}$) powders.

The change in magnetic behavior can also be attributed to the change in crystallographic phase structure resulting from compositional variation. From the theory 'local environmental effect' suggested by Kakehashi et al. [131] that nonlinear magnetic coupling between local magnetic moments of Fe results in the magnetization of Fe-Ni alloys. In a previous literature [132], it is reported that Ms of bulk iron and nickel is 222 emu/g and 55 emu/g respectively. Since BCC- Fe shows higher magnetic moment than FCC- Ni. Therefore substitution of Ni in Fe is the main reason for the decrease in Ms. As Ni content is increased, FCC phase is enhanced, and therefore Ms of the alloy is decreased. The lack

TABLE 6.2: Coercivity and saturation magnetization values of obtained Fe-Ni alloy powders.

S.No.	A-($Fe_{90}Ni_{10}$)	A-($Fe_{70}Ni_{30}$)	A-($Fe_{50}Ni_{50}$)
Hc (Oe)	4.90	6.95	28.50
Ms (emu/g)	181.4	143.8	108.6

of hysteresis loop for alloy powders suggests their soft magnetic behavior. Maximum Hc is observed in powder A-($Fe_{50}Ni_{50}$) and minimum is observed in A-($Fe_{90}Ni_{10}$). Hc $\sim$ 28.5 Oe obtained for A-($Fe_{50}Ni_{50}$) alloy powder which is much less than the previously reported [81] values for chemically synthesized and commercially available A-($Fe_{50}Ni_{50}$) alloy powder.

Kanhe et al. [133] reported that high Hc might occur due to the presence of more unpaired 3d electrons. An ordered magnetic moment or saturation magnetization of ferromagnetic transition metals is less than the predicted magnetic moment according to the Hund's rule [134]. The partial overlap of 3d orbital with 4s in the band structure decreases the unpaired electron fraction which results in the reduction of magnetic moment. The presence of unpaired 3d electrons in A-($Fe_{(100-x)}Ni_{(x)}$) system affects the magnetic moment and the fraction of unpaired electrons changes with the change in composition. Therefore it is expected that the sample having more 3d unpaired electrons fraction will show strong ferromagnetic coupling and exchange interaction. In the present case, maximum Ms is observed in A-($Fe_{90}Ni_{10}$) sample which attributes to the presence of maximum unpaired 3d electrons in this composition.

6.5 Summary of the chapter

Nano structured Fe-Ni powders with crystallite size below 50 nm are successfully synthesized using auto-combustion synthesis route followed by a thermal reduction in the hydrogen atmosphere. Single FCC (γ-Fe,Ni) phase formation is confirmed in A-($Fe_{50}Ni_{50}$) powder using Rietveld refinement with lattice parameter 3.5860$\mathring{A}$. Remaining two powders A-($Fe_{70}Ni_{30}$) and A-($Fe_{90}Ni_{10}$) were found to consist both BCC (α-Fe,Ni) and FCC (γ- Fe,Ni) phases. Spherical particles along with the smooth surfaces formed a network in all the three powders which are observed using SEM. A close observation using TEM analysis has shown the formation of nano structured spherical particles connected to each other forming a network. Increasing Ni content resulted in the agglomeration of these networks and alignment of particles in (111) direction. Maximum saturation magnetization is found in A-($Fe_{90}Ni_{10}$) due to the presence of major BCC phase. The soft magnetic behavior of powders is confirmed from high saturation magnetization and low coercivity values observed from M-H loop. This behavior is attributed to the nanocrystalline alloy formation in all three compositions.